Model Studies in Catalysis Using Surface Science Probes

D. Wayne Goodman*

Department of Chemistry, Texas A&M University, College Station, Texas 77843

Received August 5, 1994 (Revised Manuscript Received February 1, 1995)

Contents

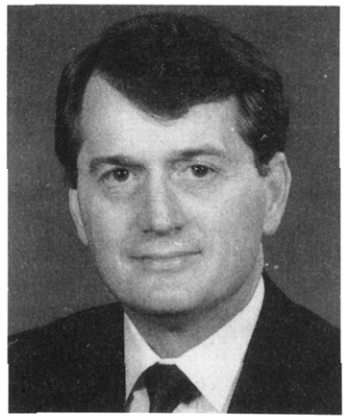

Dr. Goodman received his Ph.D. in physical chemistry from the University of Texas in 1974 and the following year, as a NATO Fellow, did postdoctoral study at the Technische Hochschule, Darmstadt, Germany. In 1976, he was chosen an NRC Research Fellow with the National Bureau of Standards where he became a member of the research staff in 1978. In 1980 he moved to Sandia National Laboratories, where he became Head of the Surface Science Division in 1985. Dr. Goodman joined the faculty of Texas A&M in 1988 as professor of chemistry and in 1994 became Welch Professor. He is the recipient of the Ipatieff Award of the American Chemical Society in 1983, the Colloid and Surface Chemistry Award of the American Chemical Society in 1993, the Harwood Medal of the British Vacuum Society in 1994, and a Humbold Research Award in 1995. He has held several lectureships including, most recently, the Ipatieff Lectureship at Northwestern University in 1993. He is the author of over 250 publications/book chapters and is an active member/officer of the American Chemical Society, American Physical Society, American Association for the Advancement of Science, American Vacuum Society, and the Materials Research Society.

I. Introduction

A key issue in catalytic research is the relationship among the atomic structure, composition, and electronic properties of a surface and catalytic activity/selectivity. Over the last several decades, a myriad of ultrahigh vacuum (UHV) surface techniques has become available to precisely define surfaces at the atomic level. Accordingly, considerable effort has been invested in applying these UHV methods to basic catalytic problems. Most surely an approach to catalytic research that combines modern surface techniques with traditional methods will enhance significantly our understanding of a broad range of phenomena that occur at surfaces with respect to catalytic reactivity and selectivity.

UHV surface science offers many new opportunities in catalytic research in that a variety of modern spectroscopies are available to study the detailed structure and composition of surfaces and to identify stable surface species. However, a criticism that has been made frequently of the UHV approach is that it is too far removed from reality, since catalytic reactions typically are carried out under quite different conditions, namely, at atmospheric (or higher) pressures and with far more complex surfaces than the single-crystal surfaces most frequently used in vacuum surface science studies. These disparities between the two areas have been referred to frequently as the "pressure and material gaps".

The so-called "pressure gap" separating UHV and technical catalytic investigations has been bridged in recent years by combining in a single apparatus the ability to measure kinetics at elevated pressures on single-crystal catalysts with the capabilities of carrying out surface analytical measurements.[1−6] In these high-pressure/surface analytical studies a well-defined, single-crystal plane is used to model a site or set of sites expected to exist on practical high-surface-area catalysts. This approach has allowed a direct comparison of reaction rates measured on single-crystal surfaces with those measured on more realistic catalysts.[7] These combined methods have also provided detailed studies of structure sensitivity, the effects of promoters/inhibitors on catalytic activity, and, in certain cases, the identification of reaction intermediates by post-reaction surface analysis.[7,8] These kinds of studies have established the validity of using single-crystal surfaces for a variety of reaction categories to model the more complex technical catalysts.

Despite these successes in modeling catalysts with single crystals, there is a clear need to develop models with higher levels of complexity to address those important issues specifically related to very small metal particles and to interactions between the metal particle and the support.[9] That is, in addition to bridging the "pressure gap", we need as well to bridge the "material gap".

This article begins with a discussion of selected examples of single-crystal work and concludes with a description of recent efforts to simulate oxide-supported metal systems. These examples illustrate the wide range of opportunities offered by model systems for studying complex issues of catalysis such as structure sensitivity/insensitivity and metal-support interactions. In the latter case, by using a model

0009-2665/95/0795-0523$15.50/0

oxide-supported metal catalyst, the nuances of the more complex "real world" system can be directly investigated while maintaining a catalytic system that is tractable for typical surface science probes.

II. Experimental

The experiments were carried out utilizing several combined ultrahigh vacuum/microreactor systems, described elsewhere,[10-11] with capabilities for X-ray and UV photoelectron spectroscopy (XPS, UPS), ion scattering spectroscopies (ISS), high-resolution electron energy-loss spectroscopy (HREELS), infrared reflection adsorption spectroscopy (IRAS), Auger electron spectroscopy (AES), low-energy electron diffraction (LEED), and temperature-programmed desorption (TPD), and facilities for sample heating and cooling.

The details for the cleaning and handling of the single-crystal catalysts are given in the appropriate related references. For the simulated supported metal catalysts, Mo(110) and Ta(100) substrates[12,13] were chosen for preparing the thin SiO_2[14,15] and Al_2O_3 films.[16] Sample temperatures were monitored with a pair of W−5%Re/W−26%Re thermocouple wires spot-welded to the edge of the rear surface. Cu and Pd were evaporated from sources containing the corresponding high-purity metal wire tightly wrapped around a tungsten filament. Scanning tunneling microscopic (STM) and atomic force microscopic (AFM) studies were performed with a Digital Instruments Nanoscope II.

III. Results and Discussion

A. Model Single-Crystal Catalysts

a. CO Methanation over Ni,Ru Single Crystals

Early studies in our laboratories[3,5,17,18] of the methanation reaction or the reaction of CO with H_2 to make methane showed that metal single crystals could be used to model reactions taking place on supported metal particles. In these studies similarities among the data for the close-packed Ni(111)[5] and Ru(001)[10,18] surfaces, the more open Ni(100)[5] and Ru(110)[18] crystal planes, and data for alumina-supported nickel particles demonstrated that the methanation reaction is indeed quite insensitive to the surface structure of nickel and ruthenium catalysts.

b. CO Oxidation over Rh, Ru, Ir, Pt, and Pd

More recently this structure insensitivity has been extended to other reactions including the CO oxidation reaction. The relative simplicity of CO oxidation makes this reaction an ideal model of a heterogeneous catalytic reaction. Each of the mechanistic steps (adsorption and desorption of the reactants, surface reaction, and desorption of products) has been probed extensively under UHV conditions with the modern techniques of surface science.[19] Because many of the reaction parameters determined in UHV can be applied directly to the kinetics at higher pressures,[20] CO oxidation to date best illustrates the continuity between UHV and elevated pressure studies.

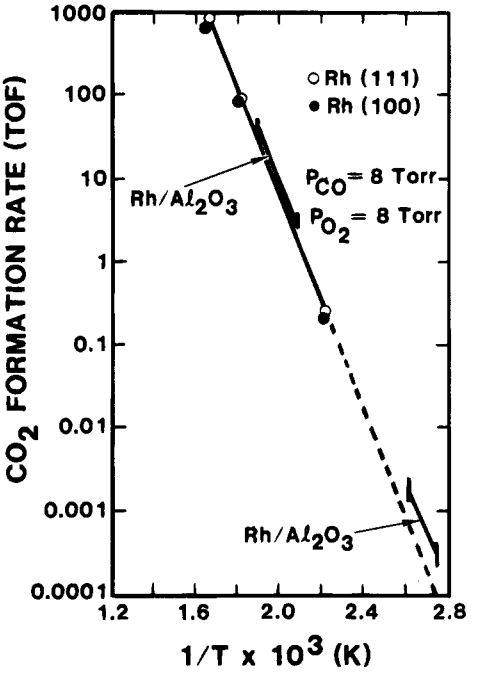

Figure 1. Comparison of the specific rates of the CO−O_2 reaction measured over Rh(111) and Rh/Al_2O_3 at $P_{CO} = P_{O_2}$ = 0.01 atm. Model predictions were obtained using two different oxygen adsorption kinetics.

Figure 1 compares specific reaction rates [(product molecules)(substrate surface atom)$^{-1}$(second)$^{-1}$] or turnover frequency (TOF) of CO oxidation measured over single crystals of Rh with those observed on supported Rh/Al_2O_3 catalysts.[20,21] There is remarkable agreement between the model and supported systems with respect to the specific reaction rates and apparent activation energies. These results show that the kinetics of CO oxidation on Rh is not sensitive to changes in catalyst surface morphology, even from bulk Rh single crystals to relatively small supported Rh particles. Under the conditions of Figure 1, the surfaces are predominantly covered with CO so that the reaction is limited by the adsorption rate of oxygen.[20,21] As the temperature is increased, the reaction rate increases because more vacant sites become available for oxygen adsorption as a result of the higher CO desorption rate. In Figure 1 the CO oxidation rate increases with temperature following an apparent activation energy very similar to that for CO desorption.

The behavior of the reaction can be analyzed by using a kinetic model established from UHV surface science studies of the interactions of CO and O_2 with Rh.[20] By using the rate constants for adsorption and desorption of CO and O_2 measured at UHV conditions, the kinetics of CO oxidation over Rh can be very accurately predicted at elevated pressures. The dashed line of Figure 1 represents the predicted Arrhenius behavior from this model.[20] This close comparison between the single-crystal results and those of the model represents an exceptional example of the continuity between UHV surface science and "real world" catalysis.

Further examples of the correspondence between model single crystals and supported metal catalysts for CO oxidation have been found for Ru,[22,23] Pt,[24] Ir,[24] and Pd.[24-26] In the case of Ru,[22,23] post-reaction

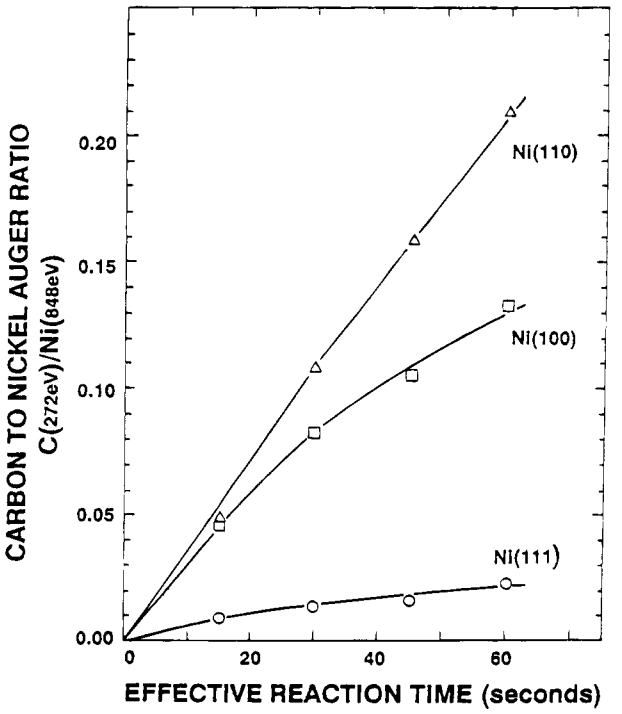

Figure 2. Methane decomposition kinetics on low index nickel single crystal surfaces at 450 K and methane pressure $P_{methane}$ of 1.00 Torr.[9]

surface analysis indicates that the optimum rate of CO oxidation on Ru(001) is observed when the surface is covered by almost a monolayer of oxygen. This surface condition contrasts with that of Rh, where the optimum activity is obtained for surfaces essentially free of oxygen adatoms.[20,21]

In contrast to methanation and CO oxidation, there are reactions whose reactivity and selectivity depend markedly on the surface geometry or the metallic particle size of the catalyst. The reactive sticking and hydrogenolysis or "cracking" of alkanes are important examples of "structure sensitive" processes.

c. Alkane Reactive Sticking on Nickel Single Crystal Surfaces

The reactive sticking of alkanes on nickel single-crystal surfaces is strongly dependent on the surface structure. For example, methane reactivity, shown in Figure 2 as the time-dependent carbon buildup from 1 Torr of methane in contact with the various low index nickel single crystal surfaces at 450 K, is seen to increase in the order Ni(111) < Ni(100) < Ni(110).[27] Initial reaction rates for the Ni(110) and Ni(100) surfaces are very similar and are ~7−10 times greater than the initial rate for Ni(111) surfaces at 450 K. However, both the Ni(100) and Ni(111) surfaces exhibit a strong coverage dependence in the methane decomposition rate, as evidenced by the deviation from linearity in the plots for these surfaces shown in Figure 2. This behavior is in contrast with that of the Ni(110) surface, which does not exhibit the same downward curvature, possibly indicating carbon islanding or a reduced carbon coverage dependence for the methane reactivity on this surface.

A comparison with the results of molecular beam studies suggests that the effects of vibrational energy on sticking probabilities must be accounted for and the sticking probabilities of molecules with very low normal kinetic energies must be accurately known when attempting to model high-pressure processes using molecular beam techniques.[27] While the dissociation of methane indicates that the "direct" channel to dissociation might dominate for certain crystal planes, e.g. Ni(111), the results for the higher alkanes imply that dissociation of these molecules proceeds primarily via a trapped molecular precursor.[28,29]

These studies on the alkane-reactive sticking on nickel single-crystal surfaces were carried out under the high incident flux conditions. The elevated pressures, in general, are required to produce measurable products, not because of the greater availability of higher velocity molecules, but rather because of the competition that is inevitably present between desorption from the precursor or adsorbed state and dissociation. Since the activation energies for desorption of many reactants of interests (particularly hydrocarbons) are frequently smaller than the activation energies for reaction, desorption dominates and reaction probabilities are quite small, often too small to measure at UHV conditions. For these reactants, the greater number of collisions at higher pressures simply serves to overcome this limitation.[28,29]

By extrapolating the rates of dissociative adsorption of alkanes measured in "thermal bath" experiments to the pressure and temperature conditions used in the hydrogenolysis and steam reforming studies, it has been found that ethane dissociation rates on the clean surface are 1−2 orders of magnitude larger than the rates of ethane hydrogenolysis and reforming and *n*-butane dissociation on the clean surface is 2−3 orders of magnitude faster than *n*-butane hydrogenolysis under comparable conditions.[28] Since the alkane dissociation rates measured in these "thermal bath" experiments are initial rates measured in the limit of zero carbon coverage, they represent a theoretical upper limit to the rates of hydrogenolysis and steam re-forming of these alkanes on unpromoted nickel catalysts.

In summary, these studies have shown a direct relationship between the atomic corrugation of a surface and its activity toward the dissociative sticking of alkanes. Since dissociative sticking is the key initial step in the hydrogenolysis of alkanes, then a similar correlation between the atomic "roughness" and activity for this reaction might be anticipated. This indeed is the case as is shown in the following section.

d. Hydrogenolysis of Small Alkanes on Nickel and Iridium Single Crystal Surfaces

The reactivity for ethane hydrogenolysis to methane on nickel has been shown to depend critically on the particular geometry of the surface. Figure 3 shows the specific reaction rates for methane formation from ethane over Ni(100) and Ni(111) surfaces plotted in Arrhenius form.[30] It can be seen that the more open (100) surface is far more active than the close-packed (111) surface. For the Ni(100) surface, the data give an apparent activation energy of 100 kJ/mol, which is remarkably close to the 105 kJ/mol

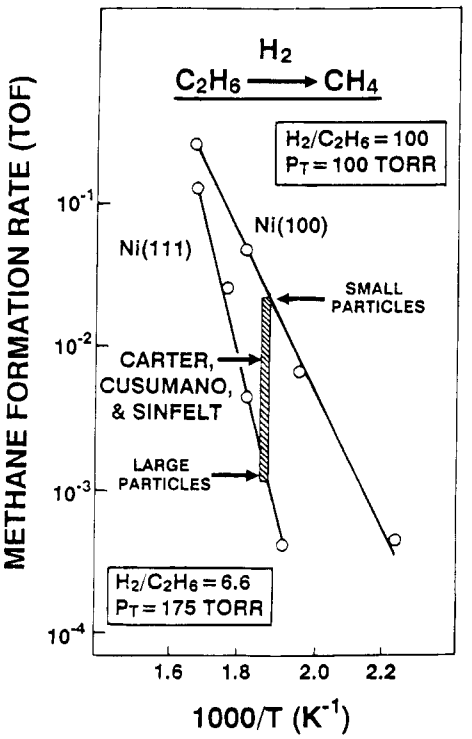

Figure 3. Arrhenius plot for ethane hydrogenolysis reaction on Ni(100) and Ni(111) surfaces at a total reactant pressure P_T of 100 Torr and $H_2/C_2H_6 = 100$.[12] Also shown is the result on supported nickel catalysts at P_T of 175 Torr and $H_2/C_2H_6 = 6.6$.[22]

obtained for the methanation reaction over the same surface.[5] Furthermore, the specific rates observed for both methanation and ethane hydrogenolysis on this surface are virtually identical for the same partial pressure of hydrogen. These observations strongly suggest that these two reactions over the Ni(100) surface are following the same reaction pathway and are limited by the same reaction step. As previously shown for the methanation reaction,[5,8] ethane hydrogenolysis on this surface must involve a surface carbon formation step followed by its reduction by hydrogen. In contrast, the kinetic data shown in Figure 3 for the Ni(111) surface give an activation energy of 192 kJ/mol, implying that a different reaction mechanism is operative.

It should be noted that surface analysis following reaction showed the (111) and (100) surfaces with comparable submonolayer quantities of carbon. Therefore preferential surface carbon formation, or self-poisoning, on the (111) surface is not responsible for its lower activity.[30]

Surfaces with (111) orientations are encountered more prevalently in FCC materials as the particle size is increased via successively higher annealing temperatures.[31] The results of this study then are consistent with rate measurements on supported nickel catalysts[32,33] which show hydrogenolysis activity to be a strong function of particle size, the larger particles exhibiting the lower rates as illustrated in Figure 3.

The selectivity for ethane production from the hydrogenolysis of *n*-butane over iridium single crystals has been demonstrated to scale with the concentration of low-coordination-number metal surface atoms.[34,35] Figure 4 shows the results on Ir(110)-(1×2) and Ir(111) surfaces as well as the schematic representation of these iridium surfaces. The Ir(110)-(1×2) surface has been found to produce ethane very selectively.[36] This contrasts with the results for the close-packed Ir(111) surface, where only the statistical scission of C−C bonds has been observed. Although there is still some controversy regarding the surface structure of Ir(110) under reaction conditions, its selectivity for ethane production is clearly superior to Ir(111). The results of this study correlate qualitatively with the observations made previously for

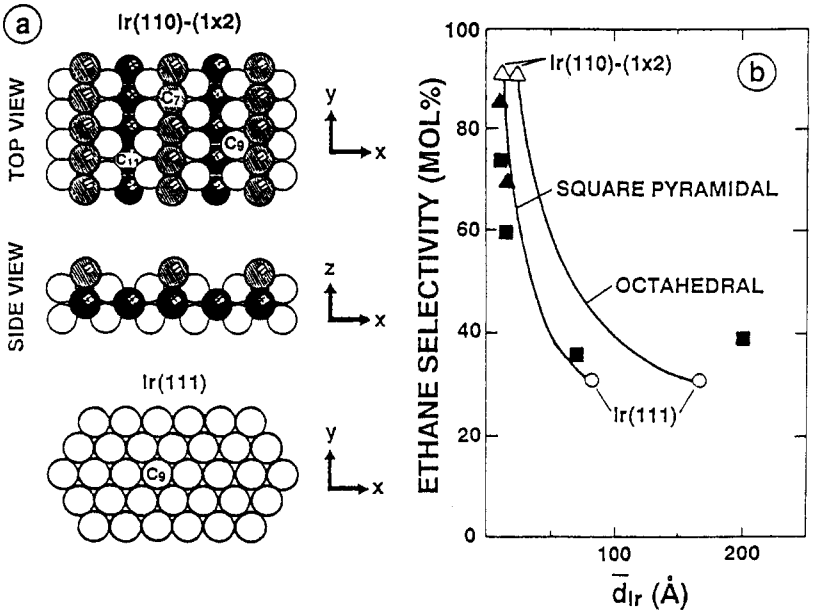

Figure 4. Diagram showing the correlation between selectivity and structure for *n*-butane hydrogenolysis on iridium. (a) Schematic representation of the Ir(110)-(1×2) and Ir(111) surfaces. The *z* axis is perpendicular to the plane of the metal surface. C_n designates the coordination numbers of the metal surface atoms. (b) Selectivity for C_2H_6 production (mol % total products) for *n*-butane hydrogenolysis on iridium single crystals[13,14] and supported iridium catalysts[26] at 475 K. The effective particle size for the single crystal surfaces is based on the specified geometrical shapes: ▲, Ir/Al_2O_3; ■, Ir/SiO_2.

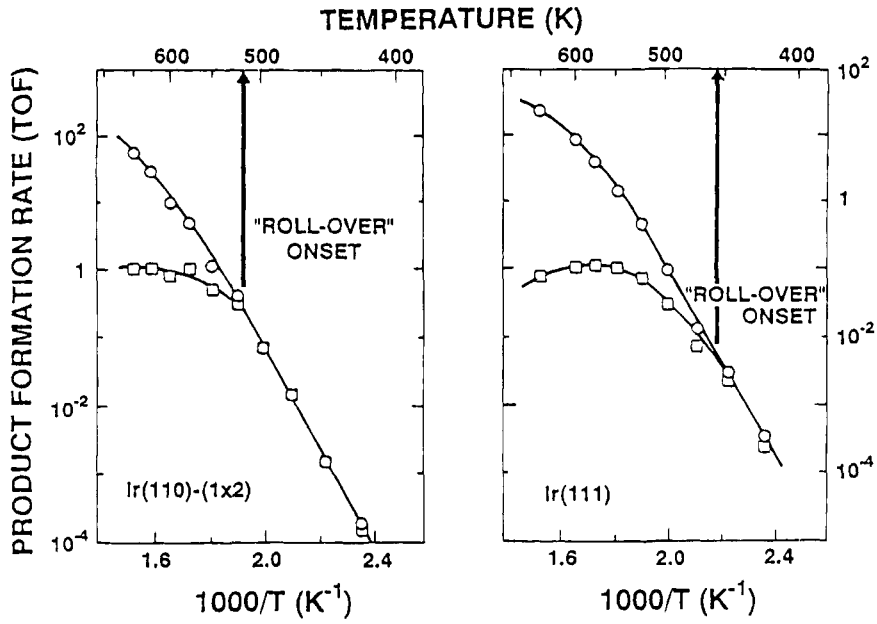

Figure 5. Arrhenius plot for propane hydrogenolysis reaction on Ir(110)-(1×2) and Ir(111) surfaces at a total reactant pressure P_T of 101 Torr and H_2/C_3H_8 = 100: ○, methane; □, ethane.

selective hydrogenolysis of *n*-butane to ethane on supported iridium catalysts as a function of iridium particle size,[37] which is also shown in Figure 4. It can be seen that the results for Ir(110)-(1×2) model very well the small-particle limit, whereas the results for Ir(111) relate more closely to the data for the corresponding large particles (>10 nm). By assuming particle shapes, the general behavior of declining selectivity with larger particle size can be accurately modeled, as illustrated in Figure 4.

The stoichiometry of the surface intermediate leading to high ethane selectivity, based on kinetics and surface carbon coverages subsequent to reaction, is suggested to be a metallocyclopentane.[34,35] The Ir(110) surface undergoes a reconstruction, described as the Ir(110)-(1×2) or "missing-row" structure, resulting in rows of the highly coordinatively unsaturated "C_7" sites, as schematically shown in Figure 4. These sterically unhindered C_7 sites can form a metallocyclopentane species (e.g., a 1,4-diadsorbed hydrocarbon species) which has been proposed as an intermediate in the central scission of butane to ethane. On the basis of analogous chemistry reported in the organometallic literature,[38,39] the mechanism responsible for the hydrogenolysis of *n*-butane on the Ir(110)-(1×2) surface has been postulated to be the reversible cleavage of the central C−C bond in this metallocyclopentane intermediate. On the other hand, butane hydrogenolysis on the Ir(111) surface appears to operate via a different mechanism. First, dissociative chemisorption of butane and hydrogen occurs followed by irreversible cleavage of the terminal carbon−carbon bond of the adsorbed hydrocarbon. Further C−C bond cleavage prior to product desorption leads to the methane and ethane observed as initial products.

For both iridium surfaces, the extent to which hydrogenolysis proceeds increases with increasing reaction temperature. This is in keeping with the general trend for increased cracking at higher temperatures for alkane reactions. The term "roll-over" has been used to describe the fall in overall activity at the high temperatures which leads to a decrease in the selectivity for the production of ethane (shown in Figure 5) in the hydrogenolysis of propane over these two iridium surfaces. Decreasing the partial pressure of H_2 at the temperature of onset of roll-over induces the same selectivity change as observed for an increase in reaction temperature. The origin of this effect is believed to be as follows. As the reaction temperature is raised beyond a critical temperature, the hydrogen surface coverage falls below a saturation or critical coverage. The lower hydrogen coverage then reduces the efficiency of the hydrogenation of surface hydrocarbon fragments. It is shown in Figure 5 that the roll-over onset occurs at a higher temperature on the Ir(110)-(1×2) than that on the Ir(111) surface. From previous studies, it is known that hydrogen desorbs at a higher temperature (390 K at the saturation of the high-temperature desorption state) from Ir(110)-(1×2) than from Ir(111) surface (255 K at 250 L of hydrogen).[40] Therefore, the higher temperature of onset of roll-over on the more open Ir(110)-(1×2) surface correlates with the higher binding energy of hydrogen adatoms on this surface. This suggests that the active chemisorbed hydrogen is present on metal sites rather than carbon-covered sites.

The atomic-level details of the "structure sensitivity" of alkane hydrogenolysis are still incomplete; however, this work shows clearly that a large component of this important catalytic effect is a structural one and relates to the partitioning of the facet distribution as a function of particle size. All of the results summarized above correlate very well with measurements on supported "real-world" catalysts and emphasize the important role that single crystal studies can play in defining relationships between surface structure and catalytic activity/selectivity.

B. Model Oxide-Supported Metal Catalysts

Although single crystals can be used successfully to model a variety of heterogeneously catalyzed reactions, there is a clear need to develop more complex models to address those important issues specifically related to very small metal particles and to interactions between the metal particle and the support.

The first challenge in the synthesis of an oxide-supported metal model catalyst is the preparation and characterization of a suitable oxide catalyst support. Unfortunately, oxide surfaces such as those frequently encountered as catalyst supports are insulating materials and present problems of varying degrees to many charged-particle surface probes. Recently the difficulty associated with surface charging has been eliminated in our laboratories by preparing an ultrathin, highly ordered, oxide film on the surface of a metal substrate. Any charging induced in the thin film during charged-particle measurements is dissipated via the conducting substrate. This section begins by describing the experimental approach to the preparation of ultrathin films of silica and alumina and then moves to the synthesis and characterization of supported metal particles of copper and palladium.

a. Preparation and Characterization of the Oxide Supports

Thin SiO_2 films have been synthesized on a Mo(110) substrate by evaporating silicon into an oxygen background. A Mo(110) single crystal was chosen as the substrate because of its relative ease of cleaning and the ability to thermally desorb the thin films of SiO_2 from the surface.[41,42]

Silicon dioxide is formed on the substrate at room temperature when silicon is evaporated in a $\sim 4 \times 10^{-6}$ Torr O_2 background.[41-43] Figure 6 shows the Auger electron spectra for the films prepared under oxygen background pressures of 0, 1×10^{-6}, and 4×10^{-6} Torr. Clearly, both silicon and silicon dioxide

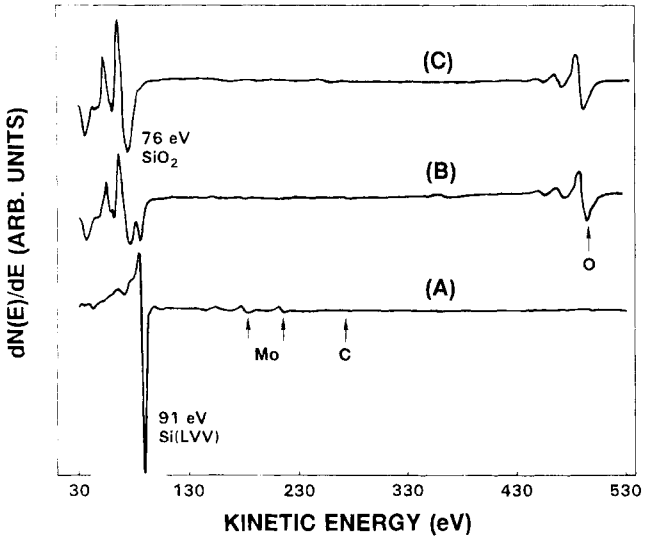

Figure 6. Auger electron spectra for thin films of silicon and silicon dioxide on Mo(110) prepared by evaporating silicon at oxygen partial pressures of (A) 0, (B) 1×10^{-6}, and (C) 4×10^{-6} Torr.

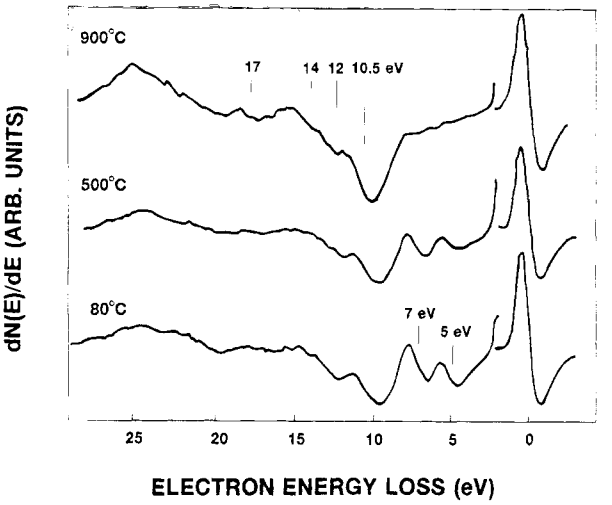

Figure 7. First-derivative electron energy loss spectra for a ~50 Å silicon dioxide film on Mo(110) annealed to 80, 500, and 900 °C. The resolution of the analyzer is ~0.6 eV.

are deposited in the intermediate oxygen pressure range of 1×10^{-6} Torr. The Auger spectra and the relative intensities of silicon and oxygen do not change for films prepared at oxygen pressure greater than 4×10^{-6} Torr, consistent with the production of only a silicon dioxide film at the higher oxygen pressure conditions. The silicon and silicon dioxide species are differentiated on the basis of their characteristic Auger transition energies and line shapes. Silicon dioxide has characteristic LVV Auger transitions at 76, 63, and 59 eV, whereas silicon has a major Si(LVV) peak at 91 eV.[43,44] In addition, an Auger transition energy of ~85 eV has been observed for the SiO species on platinum[45] and on silicon.[46]

The Auger spectra shown in Figure 6 further suggest that the silicon oxide films are stoichiometric, i.e., SiO_2. The presence of SiO (silicon monoxide) in the silicon oxide films can be ruled out on the basis of the absence of an Auger transition at ~85 eV.[45,46] Other silicon–oxygen species, such as "Si_2O" and "Si_2O_3", are not likely to be formed, since these species do not exist as stable compounds; these species have only been proposed to exist at the Si/SiO_2 interface.[47,48] Furthermore, the line shapes, the peak energies of the Auger electronics, and the electron energy loss spectra (Figure 7) are consistent with those of silicon dioxide.

Figure 7 shows the first-derivative electron energy loss spectra of the silicon dioxide films annealed to various temperatures. Vitreous silicon dioxide exhibits optical excitations at 10.3, 11.8, 14.0, 17.0, and 22–23 eV.[49] In addition, electron energy loss features at 10, 12, 14, 17, 20, and 23 eV have also been reported for thermally grown silicon dioxide on a silicon substrate.[50,51] There are no electron transitions below 10 eV for vitreous silicon dioxide.

The electron energy loss spectrum for the silicon dioxide films after annealing to 900 °C displays features identical to those of vitreous silica. The features at ~10, 12, 14, 17, and 20 eV are evident, although not well resolved. These electron energy features are attributed to interband transitions in silicon dioxide whereas the 23 eV feature is due to a bulk plasmon excitation.[52]

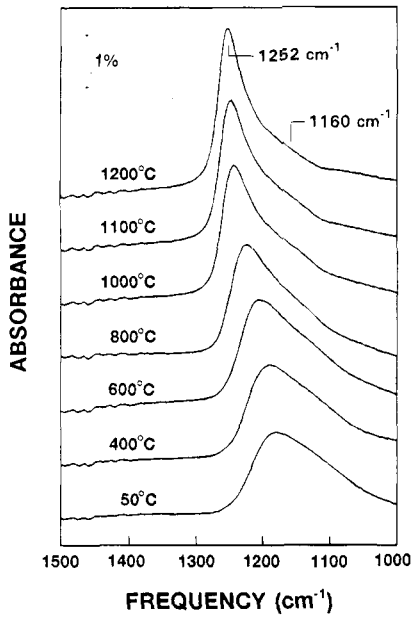

Figure 8. Infrared reflection absorption spectra for a ~50 Å silicon dioxide film on Mo(110) annealed to 50, 400, 600, 800, 1000, 1100, and 1200 °C. The spectra were acquired under ultrahigh vacuum conditions. The resolution used was 4 cm^{-1}.

The silicon oxide films prepared at room temperature exhibit additional low energy electron loss features at ~5 and 7 eV. These features are attributed to a local structure with broken Si−O bonds in tetrahedra of [SiO_4].[53] Defect-free vitreous silica consists of [SiO_4] tetrahedra connected by an oxygen bridge to form a long-range 3D network. Thus the ~5 and 7 eV EELS features indicate some smaller size [SiO_4] networks. The EELS features at 5 and 7 eV have been observed previously for silicon oxide films prepared by thermally oxidizing a silicon wafer.[51]

The intensity of the electron energy loss features at 5 and 7 eV is significantly decreased upon heating, and completely disappears after annealing to 900 °C. This behavior demonstrates that the silicon dioxide films undergo structural reorganization, eliminating the local structure with broken Si−O bonds, to form a long range 3D network of [SiO_4]. The EELS data further suggest that the silicon oxide films are stoichiometric (SiO_2) even at low temperatures.

IR reflection−absorption spectroscopy further illustrates the structural changes that occur when the silicon dioxide films are annealed (Figure 8). The asymmetric stretch motion of the Si−O bonds appears as a broad asymmetric peak centered at 1178 cm^{-1} in the IRAS spectrum for the film prepared at a substrate temperature of 50 °C. This peak gradually shifts to higher frequency upon heating the film and reaches a maximum of 1252 cm^{-1} for the silicon dioxide film annealed to 1100 °C. The features associated with the symmetric stretching (~810 cm^{-1}) and rocking (~460 cm^{-1}) vibrational modes for vitreous silica were not accessible due to the cutoff of the CaF_2 windows.

The IRAS spectra for the silicon dioxide films on the Mo(110) substrate are significantly different from those obtained using transmission IR absorption in the 1000−1300 cm^{-1} region. These differences can be attributed to the so-called Berreman effect.[54] Accordingly, the transmission IR absorption spectra for fused quartz and silicon dioxide films exhibit a strong adsorption peak at 1076 cm^{-1} with a higher wavenumber shoulder extending to 1300 cm^{-1}.[46,55] In contrast, the IRAS spectra for the silicon dioxide films do not have features at 1076 cm^{-1}. The spectra, in fact, are dominated by features above 1200 cm^{-1}. Two vibrational oscillators of asymmetric stretches (AS_1 with in-phase motion of adjacent oxygen atoms and AS_2 with out-phase motion of adjacent oxygen atoms) of silica are present in this wavenumber regime.[56] The transverse-optical (TO) and longitudinal-optical (LO) vibration modes are at 1076 (TO) and 1256 cm^{-1} (LO) for AS_1, and at 1200 (TO) and 1160 cm^{-1} (LO) for AS_2.[56,57] The TO modes are optically active, whereas the LO modes are optically inactive for an infinite crystal. These selection rules arise because the electromagnetic waves are transverse, and thus do not interact with the longitudinal phonons. However, for thin films with thickness much smaller than the wavelength of the lattice vibration, the vibrational modes normal to the surface have the frequencies of the longitudinal modes. For the vibrational modes parallel to the surface the frequencies correspond to the transverse modes.[54] Since only the vibrational modes with a component normal to the metal surface are IR active, the IRAS spectra for the silicon dioxide films exhibit only these features corresponding to the longitudinal modes. Thus the spectra from the films should differ from the corresponding spectra taken with transmission IR absorption that mainly probes the transverse features.

The increase of the peak IRAS frequency with the annealing temperature for silicon dioxide films on Mo(110) (Figure 8) suggests some ordering of films upon heating. The broad peak in the IRAS spectra for the SiO_2 films is attributed mainly to a convolution of the longitudinal optical modes of the asymmetric stretches of AS_1 (1256 cm^{-1}) and AS_2 (1160 cm^{-1}) of silicon dioxide. These two modes are coupled via *disorder* in the SiO_2 films.[56,57] The AS_2 mode is optically weak in crystalline α-quartz and its intensity increases with a concomitant decrease of the AS_1 intensity in amorphous silicon dioxide.[56] Therefore, the increase of the intensity at 1250 cm^{-1} and the decrease of the intensity at 1160 cm^{-1} strongly indicate that the SiO_2 film becomes more ordered with heating. This is also consistent with the EELS results.

Thin Al_2O_3 films were grown at room temperature on a freshly cleaned Mo(110) surface. The growth of the films was controlled at a rate of approximately one-half aluminum equivalent monolayer per minute. The background pressure of oxygen was 7×10^{-7} Torr during film growth. The films were annealed to 1200 K in oxygen ambient to improve their crystalline quality. Shown in Figure 9 are Auger spectra acquired following film synthesis at two representative film thicknesses: (a) $d_{Al_2O_3}$ = 4.4 Å and (b) $d_{Al_2O_3}$ = 20.0 Å. The thickness of the $d_{Al_2O_3}$ = 4.4 Å film was calculated from the Auger intensity ratio of the

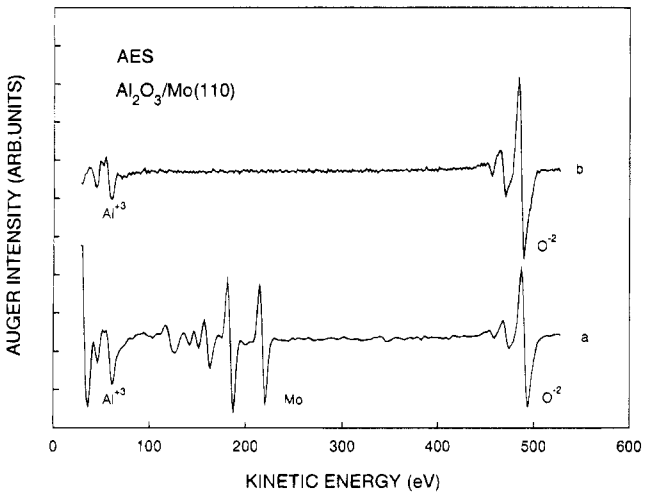

Figure 9. Auger spectra of Al_2O_3 films grown on Mo(110): (a) $d_{Al_2O_3} = 4.4$ Å; (b) $d_{Al_2O_3} = 20.0$ Å. The films were annealed to 1200 K in oxygen ambient to improve their crystalline quality. The spectra were acquired at $E_p = 2.0$ keV and at a sample current of 5 μA.

Al^{+3} (LVV) and Mo(MNN) peaks using the following equation:

$$\frac{I_{Al^{+3}}}{I_{Mo}} = \left[\frac{I_{Al^{+3}}^{\circ}}{I_{Mo}^{\circ}}\right]\left[\frac{1 - \ln\left[\frac{d_{Al_2O_3}}{\lambda_{Al^{+3}}}\right]}{\ln\left[-\frac{d_{Al_2O_3}}{\lambda_{Mo}}\right]}\right]$$

The value of $I_{Al^{+3}}^{\circ}/I_{Mo}^{\circ}$ was obtained from the standard Auger spectra of Al_2O_3 and Mo, respectively.[43] The attenuation lengths, $\lambda_{Al^{+3}}$ and λ_{Mo}, were taken from the literature to be 3.7[58] and 6.7 Å,[59] respectively. The thickness of the thick film ($d_{Al_2O_3}$ = 20.0 Å) was estimated by extrapolating the value of the thin film based on evaporation time and constant aluminum flux.

It is seen in Figure 9 that there is no indication of the presence of a metallic Al° feature at 68 eV. The predominant spectral features are the Al^{+3} (LVV) transitions at ~54 eV and the O (KLL) transition at ~500 eV. The spectral features in the 100–250 eV kinetic energy range of spectrum a arise from the Mo substrate.

Structural studies of very thin Al_2O_3 films ($d_{Al_2O_3} \leq 8$ Å) using LEED showed a complex pattern in which most diffraction spots can be interpreted as arising from electron multiple scattering at the interface. With an increase in film thickness, the multiple diffraction effects were attenuated. A simple hexagonal structure was seen at $d_{Al_2O_3} \geq 15$ Å although the diffraction spots were not as sharp as those from multiple diffraction, indicating some degree of disorder in the thick films. The lattice periodicity derived from the LEED photographs relates closely to the O–O distance in bulk Al_2O_3. The observed hexagonal pattern can therefore be interpreted as due to the presence of an ordered, close-packed oxygen anion layer associated with either the (001) orientation of α-Al_2O_3 or the (111) face of γ-Al_2O_3. A detailed structural analysis of the initial stage of epitaxy of Al_2O_3 films on a similar refractory metal substrate, Ta(110), has been given elsewhere.[16]

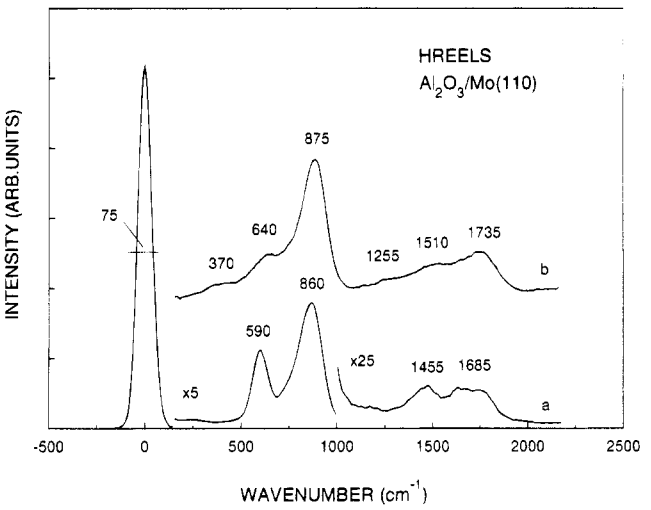

Figure 10. HREELS spectra of Al_2O_3 films grown on Mo(110): (a) $d_{Al_2O_3} = 4.4$ Å; and (b) $d_{Al_2O_3} = 20.0$ Å. The films were annealed to 1200 K in oxygen ambient to improve their crystalline quality. The spectra were acquired at E_p = 4.0 eV and at the specularly reflected beam direction.

The growth of Al_2O_3 films has been further examined using HREELS, as shown in Figure 10. The fundamental modes of the surface optical phonons (below 1000 cm^{-1} in frequency) and their multiples and combinations are evident in the spectra. The surface optical phonon losses of the thin film (spectrum a) are characterized by a two-mode pattern, whereas three modes of the phonon losses are typical for the thick film (spectrum b). These results are in a complete agreement with previous data in the literature.[60–63] Frederick et al.[64,65] have suggested that the appearance of the two phonon modes are characteristic of very thin Al_2O_3 films.

Because silica and alumina supports are widely utilized in practical catalytic applications, these oxide films are convenient materials for constructing a more realistic supported-metal–particle catalyst, intermediate in complexity between metal single crystals and the supported "real-world" catalysts.

b. Copper on Silica

Model silica-supported copper[66–68] catalysts have been prepared by evaporating copper onto a silica thin film. The preparation conditions define the corresponding metal particle dispersions or average size.[67,68] As in the studies described in the previous sections, the silica films are supported on a Mo(110) substrate.[14] The structure of the model silica-supported copper catalysts has been investigated with IRAS and scanning tunneling microscopy (STM).[66,67] The IRAS studies of adsorbed CO indicate that there are several types of copper clusters with surface structures similar to (111), (110), and other high-index planes of single-crystal copper.[66–68] The STM studies show several types of copper clusters on silica and reveal images of metal clusters on the amorphous support with atomic resolution as shown in Figure 11.[66]

c. Palladium on Silica

The adsorption and reaction of CO on model silica-supported palladium catalysts over a wide range of

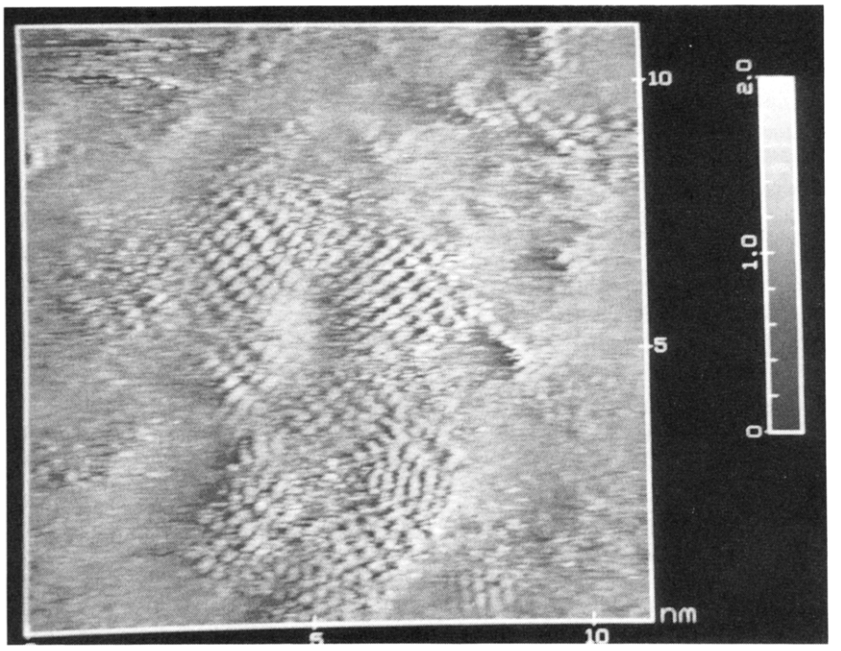

Figure 11. A STM image (110 × 110 Å) of Cu cluster formed by the deposition of 1.2 ML copper on silica(100 Å)/Mo(110). The Cluster exhibits a Cu−Cu spacing of (4.4 × 2.4) Å. This image was acquired after the sample was exposed to water and dried in air.

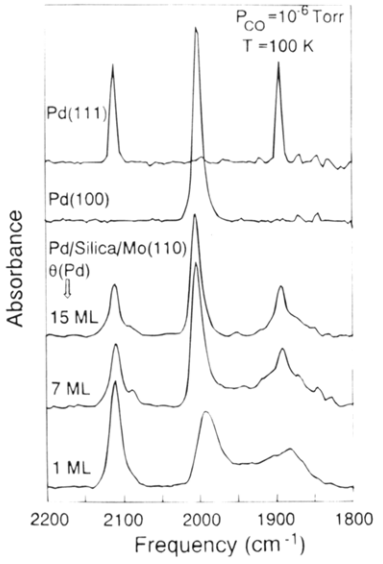

Figure 12. A Comparison of infrared reflection−adsorption spectra of CO on Pd(111), Pd(100), and silica-supported palladium surfaces. The spectra were collected at 100 K with a CO pressure of 1 × 10^{-6} Torr.

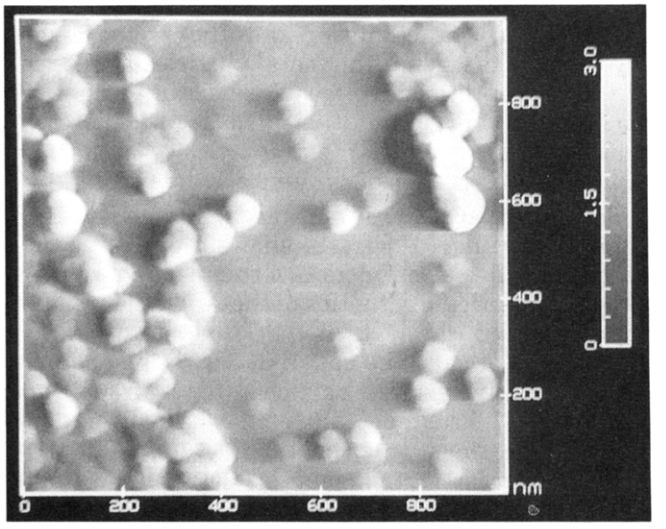

Figure 13. An atomic force micrograph of an ~10 nm SiO_2 film on Mo(100) subsequent to the deposition of 10 monolayer equivalents of palladium and an anneal to 700 K.

temperatures and pressures have demonstrated a continuity between catalysis on Pd single crystals[25,26] and Pd small particles[69−72] and, as well, between the kinetics of CO oxidation at low and high pressures. Pd overlayers of varying thickness on the thin silica films were annealed to 900 K prior to the CO adsorption experiments. This thermal treatment has been shown to produce small metal particles in the range 30−500 Å, with larger particles being formed for the higher Pd coverages.

The IR spectra of adsorbed CO on model silica supported Pd catalysts are displayed in Figure 12 for Pd coverages of 1.0, 7.0, and 15 monolayer (ML). The Pd particle size was determined by chemisorption methods[69,70] and verified using scanning probe techniques (see, for example, Figure 13). Figure 12 shows IR spectra of adsorbed CO on model Pd/SiO_2 catalysts with different Pd coverages show three distinct absorption features corresponding to CO adsorbed onto 3-fold hollow (1880 cm^{-1}), bridging (1990 cm^{-1}), and a-top (2110 cm^{-1}) configurations. At θ_{Pd} = 1.0 ML the dominant absorption feature corresponds to CO adsorbed onto an a-top position, while the peaks originating from 3-fold hollow and bridging CO are broad, suggesting a nonhomogeneous distribution of these adsorption sites. Increasing the Pd coverage to 7.0 ML and then to 15 ML results in the sharpening of the absorption features and the dominance of the peak originating from CO adsorbed in the bridging positions. These results demonstrate that the larger particles have well-defined crystal orientations, whereas the smaller particles have a wide distribution of adsorption sites. A comparison of the IR spectra of equilibrated CO overlayers obtained

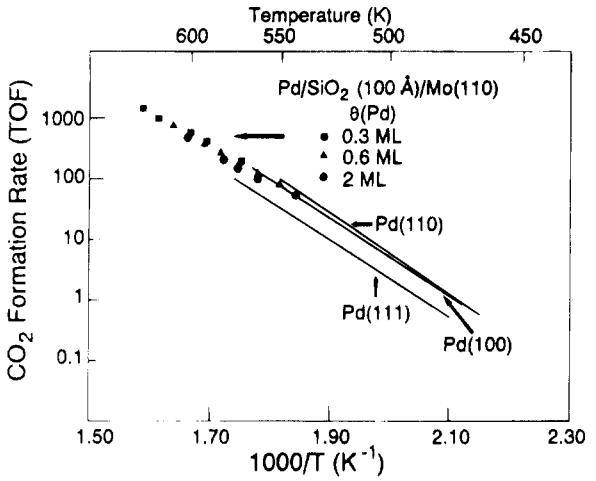

Figure 14. The Arrhenius plots of CO oxidation rate on Pd(111), Pd(110), and Pd(100) and silica-supported palladium. P_{CO} = 1.00 Torr; P_{O_2} = 0.50 Torr.

from the Pd_{15ML}/SiO_2 sample and Pd(100) and Pd(111) single crystals reveals striking similarities.[70] As Figure 12 shows, the stretching frequencies of adsorbed CO on the model Pd/SiO_2 catalyst are identical to the combined features observed for Pd(100) and Pd(111). The agreement among the IR spectra of the model supported catalysts and the metal single crystals suggests that the metal particles formed on the thin SiO_2 film have facets consisting primarily of (100) and (111) orientation. This is anticipated in that the formation of metal particles with these Miller indices is thermodynamically favored.

The oxidation of CO on this model system has been studied as well.[70] Figure 14 shows the specific CO_2 formation rates as a function of the reaction temperature. The specific activities of the single crystal and the supported catalysts for CO oxidation are essentially identical. The apparent activation energies for the relatively large particles (θ_{Pd} > 2 ML) are similar (~27 kcal/mol), but somewhat lower (~25 kcal/mol) for the smaller particles (0.6 and 0.3 ML). The apparent activation energies for three Pd single crystals with different orientations are similar[25,26,70] but distinctive [29.4 ± 0.3 kcal/mol for Pd(100), 28.1 ± 0.4 kcal/mol for Pd(111), and 30.7 ± 0.5 kcal/mol for Pd(110)]. An excellent correspondence is found among the results obtained for the model silica-supported Pd catalysts and the Pd single crystals for the oxidation of CO.

The effect of palladium particle size on the catalytic properties was investigated[71,72] utilizing the decomposition of chemisorbed NO (Figure 15) and reactions of NO with CO in flowing conditions (Figure 16). ^{15}NO was used in order to differentiate N_2 from CO and N_2O from CO_2 with mass spectrometry. During temperature-programmed reaction on the large particles following a saturation ^{15}NO exposure, ^{15}NO desorbs in three peaks centered at 315, 515, and 595 K; $^{15}N_2$ is produced in peaks at 545, 595, and 690 K; and $^{15}N_2O$ is evolved in a peak at 545 K (Figure 15A). The 545 K N_2 peak is attributed to the fragmentation of N_2O. On small palladium particles (~50 Å), $^{15}N_2O$ is not produced; ^{15}NO desorbs in two peaks at 310 and 515 K, and N_2 is evolved at 530 and 670 K (Figure 15B). The relative yield of N_2 with respect

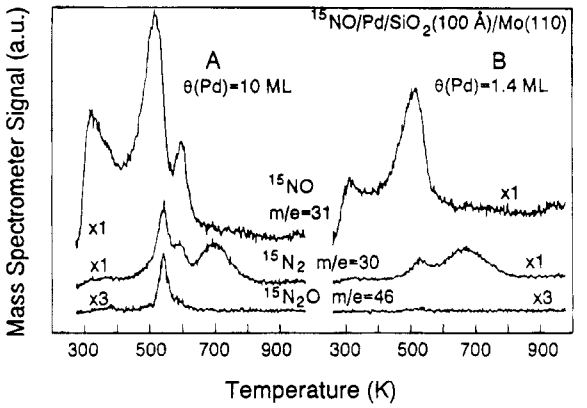

Figure 15. Temperature-programmed reaction for ^{15}NO on model silica-supported palladium catalysts. ^{15}NO was adsorbed at 290 K to saturation. The palladium coverages were (A) 10 monolayer, corresponding to a particle size of ~250 Å, and (B) 1.4 monolayer, corresponding to ~55 Å.

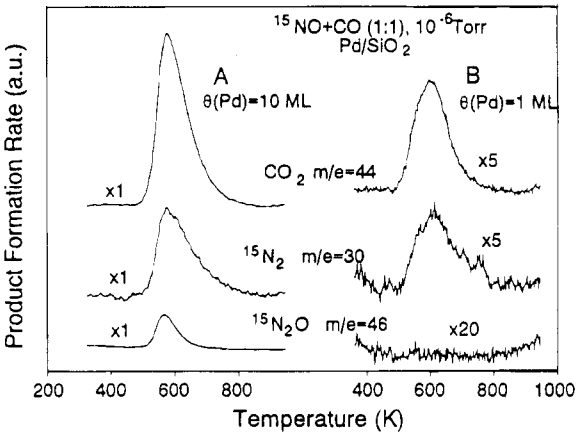

Figure 16. CO + ^{15}NO reaction rates as a function of temperature for small and large particle Pd catalysts. The gas phase pressure was 1 × 10^{-6} Torr with equimolar CO and ^{15}NO. The product formation rate was monitored via mass spectroscopy. The palladium particle sizes correspond to ~250 (A) and ~45 Å (B).

to ^{15}NO desorption (above 400 K) decreases as the particle size grows (from ~50% for 30 Å to ~20% for 250 Å particles), suggesting less NO decomposition on the larger particles. In addition, the formation of N_2O on the larger particles correlates with the appearance of the NO desorption peak at 595 K. There is no detectable O_2 evolution below 1000 K for all sizes of palladium particles. However, O_2 desorption is observed in a peak at ~1250 K, concurrent with the desorption of palladium. Therefore, the oxygen from nitric oxide decomposition is apparently dissolved into the bulk of the palladium particles.

The reaction of CO with NO under flowing conditions[71,72] further demonstrates a particle size effect (Figure 16). The relative rate of product evolution was monitored with a quadrupole mass spectrometer during reaction with flowing ^{15}NO and CO (1:1) at 1 × 10^{-6} Torr. The reaction rate increases with the catalyst temperature, reaching a maximum at ~580 K and then declines. On the large palladium particles (Figure 16A), the maximum rate of $^{15}N_2O$ evolution occurs at 570 K, 10 K lower than the maxima for both CO_2 and N_2 production. On the small particles (<50 Å), $^{15}N_2O$ is not produced during the steady-state reaction of a 1:1 mixture of ^{15}NO and

CO (Figure 16B). N_2 is produced by NO dissociation and atomic nitrogen recombination, and CO_2 is produced from the oxidation of carbon monoxide. There is a temperature (~580 K) at which the product formation rate is maximized, since the residence time for CO and NO decreases with temperature whereas the reaction rates increase with temperature.

Both the decomposition of NO and the reaction of NO with CO show that the reaction channel for N_2O formation is not available on the small particles (< 50Å). The N_2O formation requires the simultaneous presence of adsorbed NO and atomic nitrogen at sufficient coverages. The temperature-programmed reaction spectra of Figure 15 show that the dissociation of NO occurs along the trailing edge of the main NO desorption peak at 515 K. The formation of N_2O correlates with the appearance of the NO desorption peak at 595 K. The higher adsorption energy of the 595 K state increases the NO surface residence time and thus enhances the probability of N_2O formation by NO combination with atomic nitrogen. It is noted that on extended single-crystal surfaces, N_2O is also formed during the decomposition of NO.[70,73] However, the decomposition of NO and the formation of N_2O correlate with the presence of step/defect (low-coordination) sites on the single crystal surfaces.[70,73-76] Accordingly, it is likely that there are surface sites with low coordination and varying reactivities on the large particles and extended surfaces. On the perfect (111) and (100) facets, NO desorbs at <520 K,[75,76] whereas on particles with a variety of low-coordinated sites, NO can be decomposed to atomic nitrogen and oxygen on some sites, or can be more strongly adsorbed (595 K desorption state) on other sites.[71,72] The presence of both sites on the large Pd particles, a strong adsorption site for NO, and a second that promotes decomposition, provides a mechanism for the formation of N_2O. The absence of the N_2O on the small palladium particles, on the other hand, can be explained by the lack of the high-temperature NO adsorption state (595 K) which is, in turn, related to the reactivity of the surface sites. The surface of the small particles is more reactive as indicated by the increased amount of NO dissociation (~50% for 30 Å and ~20% for 250 Å particles), so that all NO molecules on the low-coordinated sites are likely decomposed to atomic oxygen and nitrogen at lower temperatures. The presence of atomic oxygen and nitrogen in the near surface region will likely further decrease the NO adsorption energy.

d. Copper on Alumina

The growth of particulate Cu deposits on these well-defined Al_2O_3 films has been studied in the 80–800 K substrate temperature range.[77] The films utilized for supporting Cu particles were typically 20 Å thick and exhibited excellent thermal stability and chemical inertness toward adsorption. It has been reported[53] that very thin Al_2O_3 films ($d_{Al_2O_3}$ < 8 Å) grown on Al substrates react with Ni deposits at elevated temperatures, causing diffusion of Ni into the substrate through defects in the Al_2O_3 film.

It has long been known[78-80] that particulate metal deposits prepared at relative low substrate temperatures exhibit smaller average particle size and higher particle density than those prepared at higher temperatures; however, the low-temperature preparations are unstable and undergo a major change in morphology and size upon annealing or chemisorption. To prepare thermally and chemically stable particles of catalytic interest, it is imperative to carry out the metal deposition at elevated substrate temperatures. Figure 17 shows a series of TPD spectra of Cu deposited onto an Al_2O_3 film at various substrate temperatures, T_s. The Cu coverages for each spectrum were adjusted to be approximately the same. Noteworthy features in Figure 17 are the shifts of the peak maxima to higher temperatures and the narrowing of the TPD peak as T_s is increased. The full width at half maximum (FWHM) of the TPD spectra, for example, decreases from ~70 K at T_s = 80 K to ~50 K at T_s = 600 K. Since the peak position and the shape of the desorption spectra determine the heat of sublimation, it is conceivable that at low substrate temperatures, the broader TPD peak contains more components and thus reflects a broader size distribution of the Cu particles. Our Auger measurements further showed that Cu particles prepared at T_s = 600 K were thermally stable up to an annealing temperature of 850 K, whereas a decrease in Cu Auger intensity was observed upon annealing for those prepared at T_s = 80 K.

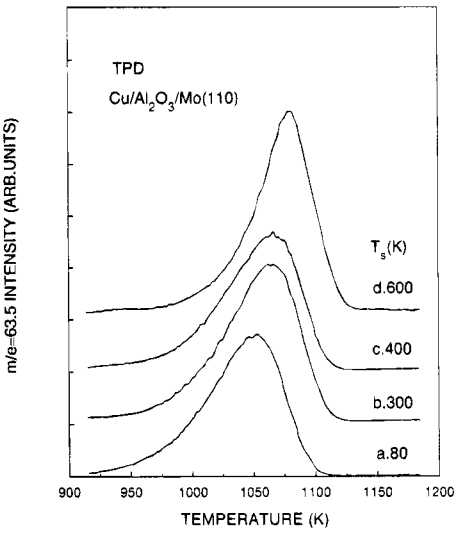

Figure 17. TPD spectra of Cu following Cu deposition on Al_2O_3 films at various substrate temperatures. The Cu coverages ($\theta_{Cu} \simeq 1.0$) for each spectrum were adjusted to be approximately the same. A linear heating rate of 10 K/s was used.

Shown in Figure 18 is a family of TPD spectra of Cu deposited at T_s = 600 K as a function of the Cu coverage in equivalent monolayers, θ_{Cu}. θ_{Cu} = 1 is defined as one monolayer (ML) of Cu on Mo(110), the coverage that can be derived from the integrated TPD area of the well-defined desorption feature of the Cu monolayer on Mo(110). Since the first monolayer of Cu grown on Mo(110) assumes the lattice structure of the substrate,[81] the surface density of one equivalent monolayer corresponds to 1.43×10^{15} cm^{-2}. The TPD spectra of Figure 18 exhibit an interesting trend in that the leading edge of the peak shifts continuously toward higher temperatures as θ_{Cu} is increased. It is also noteworthy that the TPD peak width,

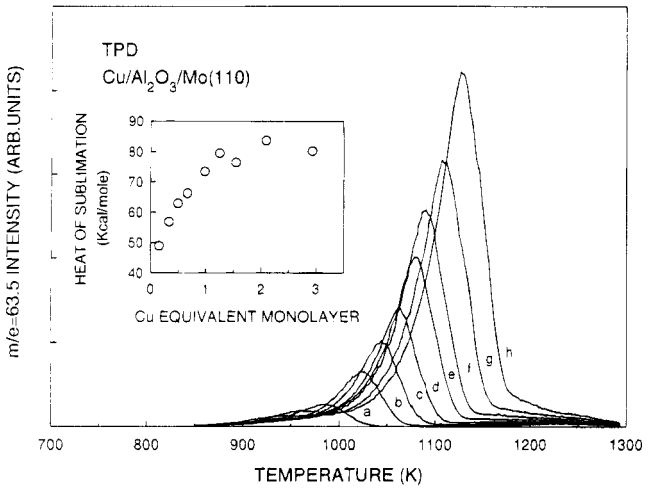

Figure 18. A family of TPD spectra of Cu deposited at T_s = 600 K as a function of equivalent monolayers, θ_{Cu}: (a) 0.16; (b) 0.33; (c) 0.50; (d) 0.67; (e) 0.98; (f) 1.25; (g) 1.55; (h) 2.09. The insert shows the heat of sublimation, derived from the leading edge analysis of the spectra, as a function of Cu coverage in equivalent monolayers. A linear heating rate of 10 K/s was used.

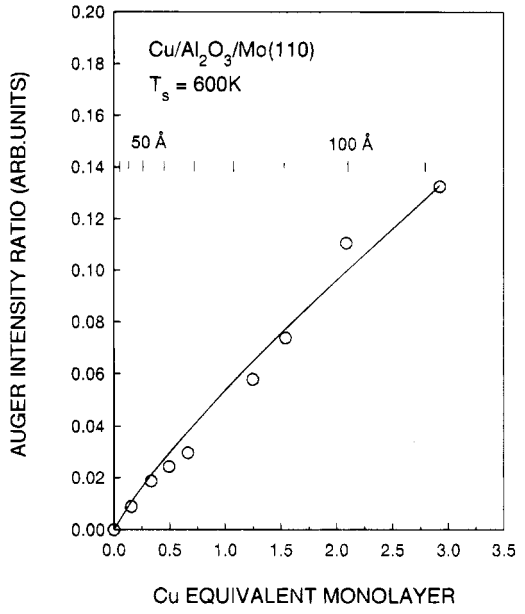

Figure 19. Auger intensity ratio of the Cu (LMM) peak to the O (KLL) peak vs the Cu coverage in equivalent monolayers. The solid line is a theoretical simulation based on the isotropic growth model, as discussed in the text. The number density of Cu particles, derived from a curve fitting procedure, is 1.4×10^{11} cm^{-2}. The average sizes of the Cu particles are inserted as vertical bars.

comparable to the width of the TPD peaks of Cu multilayers, remains approximately unchanged as θ_{Cu} is varied. The insert in Figure 18 shows the heat of sublimation, derived from the leading edge analysis[82] of the thermal desorption spectra, as a function of Cu equivalent monolayer. The heat of sublimation of Cu particles is seen to decrease rapidly from its bulk value of 80 ± 3 kcal/mol at $\theta_{Cu} \simeq 1.2$ to 49 kcal/mol at $\theta_{Cu} \simeq 0.2$. Similar behavior has been observed previously for the Cu/SiO_2 system.[67] The decrease in the heat of sublimation may be attributed to a decrease in the number of neighboring Cu atoms as the Cu particles become smaller.

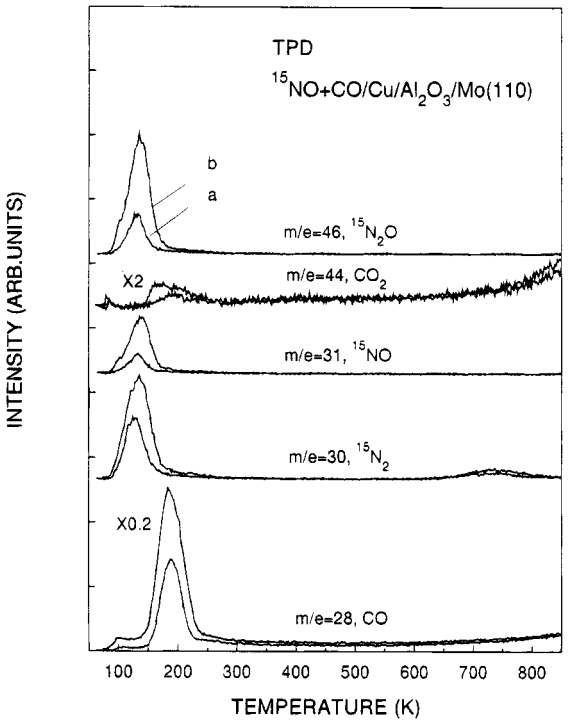

Figure 20. Thermal desorption signals for m/e = 28, 30, 31, 44, and 46 from ^{15}NO + CO adsorbed on Cu particles at 80 K vs exposure time, t: (a) t = 60 s; and (b) t = 120 s. The exposure at $t \simeq 320$ s corresponds to saturation. θ_{Cu} was 2.7, corresponding to a cluster size of ~105 Å. The ^{15}NO and CO reactants were fully mixed in the gas manifold with a ^{15}NO/CO ratio of 1:1 prior to admission into the UHV chamber. A linear heating rate of 5 K/s was used.

The average size of the Cu particles can be estimated from Auger measurements.[77] Figure 19 shows Auger intensity ratios of the Cu (LMM) peak to the O (KLL) peak versus Cu-equivalent monolayers. Each data point was collected after a fresh deposition of Cu onto the clean Al_2O_3 surface at T_s = 600 K. The solid curve through the Auger data in Figure 19 represents a theoretical simulation based on a simple model described as follows:

(1) Nucleation takes place homogeneously.

(2) After an initial nucleation period, the number of particles remains constant until the stage where coalescence sets in.

(3) The particle shape remains constant during growth.

Using the algorithm previously discussed[77] the density of Cu particles, N, can be computed from a curve fitting procedure. The calculated number of $N = 1.4 \times 10^{11}$ cm^{-2} compares favorably with those obtained by direct measurements with transmission electron microscopy (TEM): for the gold/mica system, $N = 1.0-1.5 \times 10^{11}$ cm^{-2} at T_s = 623 K;[83] for the silver/amorphous carbon system, $N = 1.0 \times 10^{11}$ cm^{-2} at T_s = 742 K.[84] The average sizes of the Cu particles, derived from a curve fitting procedure, are inserted as vertical bars in Figure 19.

The reaction of nitric oxide and carbon monoxide with particulate Cu deposits supported on Al_2O_3 films has been studied using TPD and HREELS.[77] ^{15}NO and CO reactants were fully mixed in the gas manifold with a ^{15}NO:CO ratio of 1:1 prior to admission into the UHV chamber. The adsorption of the

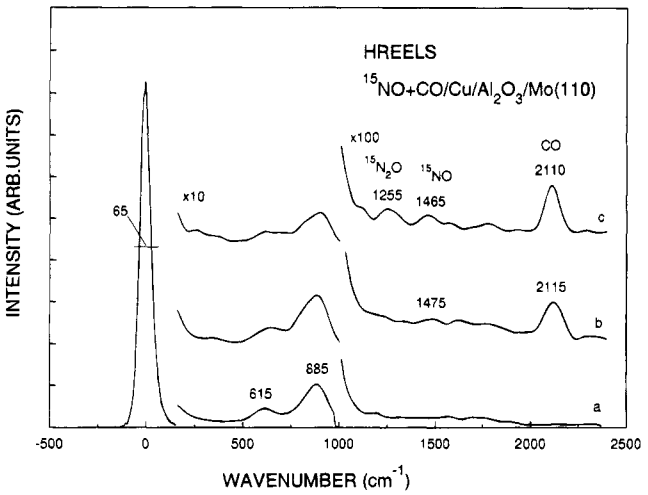

Figure 21. HREELS spectra of (a) a clean Al_2O_3 film, $d_{Al_2O_3} = 8$ Å; (b) Cu/Al_2O_3, $d_{Al_2O_3} = 8$ Å, $\theta_{Cu} = 0.67$, following a saturation exposure of $^{15}NO + CO$ at 80 K; and (c) Cu/Al_2O_3, $d_{Al_2O_3} = 8$ Å, $\theta_{Cu} = 2.7$, following a saturation exposure of $^{15}NO + CO$ at 80 K. The ^{15}NO and CO reactants were fully mixed in the gas manifold with a $^{15}NO/CO$ ratio of 1:1 prior to admission into the UHV chamber. The spectra were acquired using an electron beam with a primary energy of $E_p \simeq 42$ eV and at the specularly reflected beam direction.

gas mixture was then carried out via a gas doser at $T_s = 80$ K. Thermal desorption products from $^{15}NO + CO$ adsorbed on the Cu particles have been followed by monitoring several masses ($m/e = 28$, 30, 31, 32, 44, and 46). Shown in Figure 20 are desorption signals for $m/e = 28$, 30, 31, 44, and 46 following two different exposures. θ_{Cu} in Figure 20 was 2.7, corresponding to a cluster size of ~105 Å. No desorption signal for $m/e = 32$ was observed in the 80–850 K temperature range, indicating the absence of gaseous O_2 product. The desorption of the parent molecules of ^{15}NO and CO and the gaseous products $^{15}N_2$ and $^{15}N_2O$, due to ^{15}NO decomposition, are evident in Figure 20. The observation of a small CO_2 desorption peak ($m/e = 44$) at temperatures between approximately 150 and 250 K in the TPD spectra of Figure 20 is a clear indication for the reaction between CO and ^{15}NO on the supported Cu particles. At $\theta_{Cu} \leq 0.67$, however, the CO_2 desorption peak (not shown here) was not observed. Since the CO_2 yield is very small, the effects of particle size on CO_2 production is still unclear.

The adsorption of $^{15}NO + CO$ on particulate Cu deposits has also been studied using HREELS.[77] Shown in Figure 21 are HREELS spectra acquired following a saturation exposure of $^{15}NO + CO$ ($^{15}NO/CO = 1:1$). For reference, the spectrum of the clean Al_2O_3 surface is also included. Exposure of the clean surface to the $^{15}NO/CO$ gas mixture gives rise to several adsorbate loss features in the 1000–2500 cm^{-1} frequency range. Very similar to ^{15}NO adsorption, the 1255 and 1465 cm^{-1} losses are attributed to the $\nu(^{15}NO)$ mode of adsorbed ^{15}NO and $^{15}N_2O$, respectively. The loss peak at 2110 cm^{-1} is due to excitation of the carbon-oxygen stretch, $\nu(CO)$, of adsorbed CO.

IV. Conclusions

An approach that combines ultrahigh vacuum surface analytical methods with an elevated pressure reactor can provide new information about the molecular details that define and control the mechanism of reactions at the gas/solid interface. By using these techniques, basic concepts of heterogeneous catalysis such as structure insensitivity and structure sensitivity can be directly addressed. For structure-insensitive reactions excellent agreement can be obtained between studies on single-crystal surfaces and studies on the corresponding high-surface-area supported catalysts, demonstrating the relevance of kinetics measured on well-ordered single-crystal surfaces for modeling the behavior of practical catalysts. For structure-sensitive reactions, the activity of a particular site or set of sites can be examined and the effects of surface structure explored in atomic detail.

Recent studies have shown that model oxide surfaces can be prepared in thin-film form, a preparation that readily enables their exploration with a wide array of charged-particle surface techniques. The addition of metals to the above oxides as supports provides a convenient method to model important aspects of supported metal catalysts such as support–particle interactions and particle size effects. Using such models a host of surface science techniques can be utilized to study catalysis by metals in systems with well-defined particle sizes and morphologies.

V. Acknowledgments

We acknowledge with pleasure the support of this work by the Department of Energy, the Office of Basic Sciences, the Division of Chemical Sciences, and the Robert A. Welch Foundation.

VI. References

(1) Kahn, D. R.; Petersen, E. E.; Somorjai, G. A. *J. Catal.* **1974**, *34*, 294.
(2) Sexton, B. A.; Somorjai, G. A. *J. Catal.* **1977**, *46*, 167.
(3) Goodman, D. W.; Kelley, R. D.; Madey T. E.; Yates, J. T., Jr. *Proc. of Symposium on Advances in Fischer-Tropsch Chemistry*; American Chemical Society: Anaheim, CA, 1978.
(4) Bonzel, H. P.; Krebs, H. J. *Surf. Sci.* **1980**, *91*, 499.
(5) Goodman, D. W.; Kelley, R. D.; Madey T. E.; Yates, J. T., Jr. *J. Catal.* **1980**, *63*, 226.
(6) Campbell, C. T.; Paffett, M. T. *Surf. Sci.* **1984**, *139*, 396.
(7) Rodriguez, J. A.; Goodman, D. W. *Surf. Sci. Rep.* **1991**, *14*, 1.
(8) Goodman, D. W. *Annu. Rev. Phys. Chem.* **1986**, *37*, 425.
(9) Vannice, M. A.; Garten, R. L. *J. Catal.* **1979**, *56*, 236.
(10) Campbell, R. A.; Goodman, D. W. *Rev. Sci. Instrum.* **1992**, *63-(1)*, 172.
(11) Szanyi, J.; Goodman, D. W. *Rev. Sci. Instrum.* **1993**, *64(8)*, 2350.
(12) Wu, M.-C.; Corneille, J. S.; Estrada, C. A.; He J.-W.; Goodman, D. W. *Chem. Phys. Lett.* **1991**, *182*, 472.
(13) Wu, M.-C.; Estrada, C. A.; Corneille, J. S.; Goodman, D. W. *J. Chem. Phys.* **1992**, *96*, 3892.
(14) Xu, X.; Goodman, D. W. *Appl. Phys. Lett.* **1992**, *61(7)*, 774.
(15) Xu, X.; Goodman, D. W. *Surf. Sci.* **1993**, *282*, 323.
(16) Chen, P. J.; Goodman, D. W. *Surf. Sci.* **1994**, *312*, L767.
(17) Goodman, D. W.; White, J. M. *Surf. Sci.* **1979**, *90*, 201.
(18) Kelley, R. D.; Goodman, D. W. *Surface Sci.* **1982**, *123*, L743.
(19) Engel, T.; Ertl, G. *The Chemical Physics of Solid Surfaces and Heterogeneous Catalysis*; King, D. A., Woodruff, D. P., Eds. Elsevier: Amsterdam, 1982; Vol. 4.
(20) Oh, S. H.; Fischer, G. B.; Carpenter, J. E.; Goodman, D. W. *J. Catal.* **1986**, *100*, 360.
(21) Berlowitz, P. J.; Goodman, D. W.; Peden, C. H. F.; Blair, D. S. *J. Phys. Chem.* **1988**, *92*, 1563.
(22) Goodman, D. W.; Peden, C. H. F. *J. Phys. Chem.* **1986**, *90*, 4839.

(23) Peden, C. H. F.; Goodman, D. W. *J. Phys. Chem.* **1986**, *90*, 1360.
(24) Berlowitz, P. J.; Peden, C. H. F.; Goodman, D. W. *J. Phys. Chem.* **1988**, *92*, 5213.
(25) Szanyi, J.; Goodman, D. W. *J. Phys. Chem.* **1994**, *98*, 2972.
(26) Szanyi, J.; Kuhn, W. K.; Goodman, D. W. *J. Phys. Chem.* **1994**, *98*, 2978.
(27) Beebe, T. P., Jr.; Goodman, D. W.; Kay, B. D.; Yates, J. T., Jr. *J. Chem. Phys.* **1987**, *87*, 2305–2315.
(28) Sault, A. G.; Goodman, D. W. *J. Chem. Phys.* **1988**, *88*, 7232–7239. Sault, A. G.; Goodman, D. W. In *Molecule-Surface Interactions*, Lawley, K., Ed.; Advances in Chemical Physics; John Wiley & Sons: England, 1989; Vol. LXXVI.
(29) Goodman, D. W. *Catal. Today* **1992**, *12*, 189. Jiang, X.; Goodman, D. W. *Applied Physics A* **1990**, *51*, 99. Jiang, X.; Goodman, D. W. *Catal. Lett.* **1990**, *4*, 173–180.
(30) Goodman, D. W. *Surf. Sci.* **1982**, *123*, L679-L685.
(31) Clarke, J. K. A.; Rooney, J. J. *Adv. Catal.* **1976**, *25*, 125–183.
(32) Carter, J. L.; Cusumano J. A.; Sinfelt, J. H. *J. Phys. Chem.* **1966**, *70*, 2257–2263.
(33) Martin, G. A. *J. Catal.* **1979**, *60*, 452–459.
(34) Engstrom, J. R.; Goodman, D. W.; Weinberg, W. H. *J. Am. Chem. Soc.* **1986**, *108*, 4653–4655.
(35) Engstrom, J. R.; Goodman, D. W.; Weinberg, W. H. *J. Am. Chem. Soc.* **1988**, *110*, 8305–8319.
(36) Chan, C.-M.; Van Hove, M. A.; Weinberg W. H.; Williams, E. D. *Surf. Sci.* **1980**, *91*, 440–448.
(37) Foger, K.; Anderson, J. R. *J. Catal.* **1979**, *59*, 325–339.
(38) Grubbs, R. H.; Miyashita, A. *J. Am. Chem. Soc.* **1978**, *100*, 1300–1302.
(39) Grubbs, R. H.; Miyashita, A.; Liu, M.; Burk, P. *J. Am. Chem. Soc.* **1978**, *100*, 2418–2425.
(40) Szuromi, P. D.; Engstrom, J. R.; Weinberg, W. H. *J. Chem. Phys.* **1984**, *80*, 508–517.
(41) Xu, X.; Goodman, D. W. *Appl. Phys. Lett.* **1992**, *61(7)*, 774.
(42) Xu, X.; Goodman, D. W. *Surf. Sci.* **1993**, *282*, 323.
(43) Davis, L. E.; MacDonald, N. C.; Palmberg, P. W.; Riach G. E.; Weber, R. E. *Handbook of Auger Electron Spectroscopy*; Physical Electronics Division, Perkin Elmer: Eden Prairie, MN, 1976.
(44) Joyce, B. A.; Neave, J. H. *Surf. Sci.* **1971**, *27*, 499.
(45) Ko, C. S.; Gorte, R. J. *Surf. Sci.* **1985**, *155*, 296.
(46) Derrien, J.; Commandré, M. *Surf. Sci.* **1982**, *118*, 32.
(47) Braun, W.; Kuhlenbeck, H. *Surf. Sci.* **1987**, *180*, 279.
(48) Bianconi, A.; Bauer, R. S. *Surf. Sci.* **1980**, *99*, 76.
(49) Phillip, H. R. *J. Phys. Chem. Solids* **1971**, *32*, 1935.
(50) Ibach, H.; Rowe, J. E. *Phys. Rev. B* **1974**, *9*, 1951.
(51) Adachi, T.; Helms, C. R. *Appl. Phys. Lett.* **1979**, *35*, 199.
(52) Olivier, J.; Faulconnier, P.; Poirier, R. in *The Physics of SiO_2 and Its Interfaces*; Pantelides, S. T., Ed.; Pergamon Press: New York, 1978; pp 89–93.
(53) Liseke, N.; Hezel, R. *Thin Solid Films* **1979**, *61*, 217.
(54) Berreman, D. W. *Phys. Rev.* **1963**, *130*, 2193.
(55) Almeida, R. M.; Pantano, C. G. *J. Appl. Phys.* **1990**, *68*, 4225.
(56) Kirk, C. T. *Phys. Rev. B* **1988**, *38*, 1255.
(57) Lange, P. *J. Appl. Phys.* **1989**, *66*, 201.
(58) Chen, J. G.; Crowell, J. E.; Yates, J. T., Jr. *Phys. Rev. B* **1987**, *35*, 5299.
(59) Battye, F. L.; Jenkin, J. G.; Liesegang, J.; Leckey, R. C. G. *Phys. Rev. B* **1974**, *9*, 2887.
(60) Erskine, J. L.; Strong, R. L. *Phys. Rev. B* **1982**, *25*, 5547.
(61) Strong, R. L.; Firey, B.; de Wette, F. W.; Erskine, J. L. *Phys. Rev. B* **1982**, *26*, 3483.
(62) Crowell, J. E.; Chen, J. G.; Yates, J. T., Jr. *Surf. Sci.* **1986**, *165*, 37.
(63) Chen, P. J.; Colaianni, M. L.; Yates, J. T., Jr. *Phys. Rev. B* **1990**, *41*, 8025.
(64) Frederick, B. G.; Apai G.; Rhodin, T. N. *J. Electron Spectrosc. Relat. Phenom.* **1990**, *54/55*, 415.
(65) Frederick, B. G.; Apai G.; Rhodin, T. N. *Phys. Rev. B* **1991**, *44*, 1880.
(66) Xu, X.; Vesecky, S. M.; Goodman, D. W. *Science* **1992**, *258*, 788.
(67) Xu, X.; He, J.-W.; Goodman, D. W. *Surf. Sci.* **1993**, *284*, 103.
(68) Xu, X.; Goodman, D. W. *J. Phys. Chem.* **1993**, *97*, 683.
(69) Xu, X.; Goodman, D. W. *J. Phys. Chem.* **1993**, *97*, 7711.
(70) Xu, X.; Szanyi, J.; Xu, Q.; Goodman, D. W. *Catal. Today* **1994**, *21*, 57.
(71) Xu, X.; Chen, P.; Goodman, D. W. *J. Phys. Chem.* **1994**, *98*, 9242.
(72) Xu, X.; Goodman, D. W. *Catal. Lett.* **1994**, *24*, 31.
(73) Davies, P. W.; Lambert, R. M. *Surf. Sci.* **1981**, *110*, 227.
(74) Schmick, H. D.; Wassmuth, H. W. *Surf. Sci.* **1982**, *123*, 471.
(75) Jorgensen, S. W.; Canning, N. D. S.; Madix, R. J. *Surf. Sci.* **1987**, *179*, 322.
(76) Wickham, D. T.; Banse, B. A.; Koel, B. E. *Surf. Sci.* **1991**, *243*, 83.
(77) Wu, M.-C.; Goodman, D. W. *J. Phys. Chem.* **1994**, *98*, 9874.
(78) Poppa, H. *Catal. Rev.-Sci. Eng.* **1993**, *35*, 359.
(79) Poppa, H. *Vacuum* **1984**, *34*, 1081.
(80) Poppa, H. *Ultramicroscopy* **1983**, *11*, 105.
(81) Tikhov, M.; Stolzenberg, M.; Bauer, W. *Phys. Rev. B* **1987**, *36*, 8719.
(82) de John, A. M.; Niemantsverdriet, J. W. *Surf. Sci.* **1990**, *233*, 355.
(83) Lee, E. H.; Poppa, H.; Pound, G. M. *Thin Solid Films* **1976**, *32*, 229.
(84) Poppa, H. *J. Appl. Phys.* **1967**, *38*, 3883.

CR940027Z